FEM-Circuit co-simulation of superconducting synchronous wind generators connected to a DC network using the homogenized J-A formulation of the Maxwell equations

Wilder Durante-Gómez, Frederic Trillaud, Gabriel Dos Santos, Felipe Gonzalez-Montañez, Ghazi Hajiri, Kévin Berger, Javier de la Cruz-Soto

To cite this version:

Wilder Durante-Gómez, Frederic Trillaud, Gabriel Dos Santos, Felipe Gonzalez-Montañez, Ghazi Hajiri, et al.. FEM-Circuit co-simulation of superconducting synchronous wind generators connected to a DC network using the homogenized J-A formulation of the Maxwell equations. Superconductor Science and Technology, 2024, 37 (6), pp.065021. 10.1088/1361-6668/ad4a2f . hal-04574084v2

HAL Id: hal-04574084
https://hal.science/hal-04574084v2

Submitted on 28 Oct 2024

Superconductor Science and
Technology

ACCEPTED MANUSCRIPT

FEM-Circuit co-simulation of superconducting synchronous wind generators connected to a DC network using the homogenized J-A formulation of the Maxwell equations

To cite this article before publication: Wilder Durante-Gómez *et al* 2024 *Supercond. Sci. Technol.* in press https://doi.org/10.1088/1361-6668/ad4a2f

Manuscript version: Accepted Manuscript

Accepted Manuscript is “the version of the article accepted for publication including all changes made as a result of the peer review process, and which may also include the addition to the article by IOP Publishing of a header, an article ID, a cover sheet and/or an ‘Accepted Manuscript’ watermark, but excluding any other editing, typesetting or other changes made by IOP Publishing and/or its licensors”

This Accepted Manuscript is **© 2024 IOP Publishing Ltd**.

During the embargo period (the 12 month period from the publication of the Version of Record of this article), the Accepted Manuscript is fully protected by copyright and cannot be reused or reposted elsewhere.

As the Version of Record of this article is going to be / has been published on a subscription basis, this Accepted Manuscript will be available for reuse under a CC BY-NC-ND 3.0 licence after the 12 month embargo period.

After the embargo period, everyone is permitted to use copy and redistribute this article for non-commercial purposes only, provided that they adhere to all the terms of the licence https://creativecommons.org/licences/by-nc-nd/3.0

Although reasonable endeavours have been taken to obtain all necessary permissions from third parties to include their copyrighted content within this article, their full citation and copyright line may not be present in this Accepted Manuscript version. Before using any content from this article, please refer to the Version of Record on IOPscience once published for full citation and copyright details, as permissions may be required. All third party content is fully copyright protected, unless specifically stated otherwise in the figure caption in the Version of Record.

View the article online for updates and enhancements.

This content was downloaded from IP address 193.50.135.4 on 14/05/2024 at 15:19

FEM-Circuit co-simulation of superconducting synchronous wind generators connected to a DC network using the homogenized J-A formulation of the Maxwell equations

W. Durante-Gómez[1], **F. Trillaud**[2,6], **G. dos Santos**[3,4], **F. Gonzalez-Montañez**[5], **G. Hajiri**[6], **K. Berger**[6], **J. de la Cruz-Soto**[7]

[1]Programa de Maestría y Doctorado en Ingeniería Eléctrica, Universidad Nacional Autónoma de México, 04510 CDMX, México
[2]Instituto de Ingeniería, Universidad Nacional Autónoma de México, 04510 CDMX, México
[3]Electrical Engineering Department, Rio de Janeiro State University, Rio de Janeiro, 20550-900, Rio de Janeiro, Brazil
[4]Electrical Engineering Department, Rio de Janeiro Federal University, Rio de Janeiro, 21941-853 Rio de Janeiro, Brazil
[5]Departamento de Energía, Universidad Autónoma Metropolitana, 02200 CDMX, México
[6]Groupe de Recherche en Energie Electrique de Nancy (GREEN), Université de Lorraine, 54518 Nancy, France
[7]Instituto Tecnológico de Sonora, 85000 Ciudad de Obregón, Sonora, México

E-mail: `ftrillaudp@ii.unam.mx`

Abstract. High-temperature superconductors (HTS) are greatly appealing for the development of high efficient, and high energy density power devices. They are particularly relevant for applications requiring light and compact machines such as wind power generation. In this context, to ensure the proper design of the superconducting machines and their reliable operation in power systems, it is then important to develop models that can accurately include their physics but also can describe properly their interaction with the system. To achieve such a goal, one approach is the co-simulation. This numerical technique can bring fine geometrical and physical details of the machines through a Finite Element Model (FEM) meanwhile dealing with the operation of the whole system that incorporates the machine and a subset of the power grid represented by an external electrical circuit. The goal of the present work is to put to use this numerical technique when superconducting components are involved. Here, a case study is proposed involving a 15 MW hybrid superconducting synchronous generator (HTS rotor and conventional stator) coupled to a direct current (DC) network via a rectifier and its associated filter. The case study related to wind power application allows grasping the technical issues when employing co-simulation dealing with HTS machines. The FEM of the generator is done in the commercial software COMSOL Multiphysics, which interacts with the circuit simulator Simulink through the built-in Functional Mock-up Unit (FMU). For the present study, a new version of the latest **J**-**A** formulation combined with homogenization technique is introduced allowing an even faster computation time compared to the **T**-**A** formulation. Distributed variables and global variables such as current density, magnetic flux density, and local losses for the former and voltage, current, electromagnetic torque, and power quality for the latter are estimated and compared for both formulations. The idea is to find the best-suited combination FEM-circuit under criteria of computational speed, accuracy, and numerical stability. Thus, it is shown that all formulations generate an error of less than 5% on the machine parameters and that the **J**-**A** formulation with first order elements stands out with a significant 4-fold reduction in computational costs.

Keywords: Circuit analysis, Co-simulation, Finite element analysis, HTS generators

Submitted to: *Supercond. Sci. Technol.*

1. Introduction

Renewable energy sources, such as wind power, have gained significant attention in recent years due to their potential to mitigate climate change and to reduce dependence on fossil fuels. As wind turbines play a crucial role in harnessing wind energy, the efficiency and reliability of their generators are of paramount importance. In this regard, High-Temperature Superconductor Generators (HTSG) have emerged as a promising technical-economical solution to the implementation of wind farms [1, 2]. Thus, the commercial high-temperature superconductors (HTS) are strong candidates for the development of future large electrical machines due to their high energy density and low AC losses, resulting in enhanced efficiency at a lighter, and more compact designs than traditional machines [3]. These attributes have instigated extensive researches across various applications, driving forward the evolution of superconducting electrical machines as a promising technology to yield significantly advances in power generation and distribution systems [4]. One of the key aspects of the development of HTS machines is the ability to demonstrate their reliable operation in power grids [5]. Therefore, accurate models should be developed to study the intrinsic operation of those machines relying on the details of the electromagnetic behavior of the superconductor subjected to diverse operating conditions that result from their interaction with the power system. It is not a simple problem and proposals relying on lumped-parameter and equivalent circuit models have been developed to address this problematic [6]. Nevertheless, to understand the operation of such high-end HTS rotating machines and for their optimal design, the classic tool remains the finite element analysis [7, 8]. Modern finite element software can nowadays be easily coupled to circuit simulator [9–11], and different regimes of rotating machines can be simulated alongside their connection with the electrical network [12, 13].

In the context of HTS modeling, finite element modeling has been widely accepted as the tool to simulate large-scale HTS devices. Indeed, a FEM can easily handle refined geometrical details, not usually contemplated by equivalent circuit, as well as the nonlinear electromagnetic behavior of the HTS [14] and the ferromagnetic material (B-H curve) in the case of electrical machines. Moreover, for gaining on computation speed, various mixed formulations of the Maxwell equations have been tested thus far [15, 16]. The idea here is to use the two latest formulations, namely the **T**-**A** [8, 17, 18] and **J**-**A** formulations [19]. It is assumed that the former provides a valid reference for fast computation time and accuracy to the newest **J**-**A** formulation since it was successfully cross-checked against the well-established **H** formulation [20]. By combining these formulations with homogenization technique [18], such models are computationally fast demonstrating great success to simulate the distribution of current density and losses in coils made of thousands of turns of thin-strip HTS tapes [21].

Despite the remarkable achievements of the FEM, it is not alone sufficient to simulate complex circuits involved in power systems [13]. It is therefore appealing to couple the FEM with other numerical tools dedicated to circuit analysis. It should be mentioned that most modern finite element solvers include the ability to internally be coupled with circuits. However, it becomes quickly difficult to build within the tool a complex system dealing with several distinct components with more realistic and non-ideal characteristics. To overcome a single tool limitation, it is possible to use dedicated solvers that can be coupled together, each solver having a specialized field of applications. This is the basis of the co-simulation. For instance, the machine is modeled using FEM whereas the system, including the machine itself, is simulated using a grid simulator. This approach allows modeling a full system to account properly for varying loads making a more realistic environment for assessing the performance of the HTS tape within the machine and the machine itself [22]. Such possibility is given by coupling the commercial software COMSOL Multiphysics with Simulink of MATLAB. Some previous efforts have been carried out in that direction, see [23–26]. Nevertheless, the co-simulation technique presents some challenges for modeling HTS devices. These challenges arise from the highly nonlinear and strongly multi-physical nature of the superconductor combined with the numerical complexity of dealing with distributed solvers; a specific FEM solver for simulating the machine and a distinct solver for the circuit simulator [27]. Both segregated solvers exchange variables over the course of the time-dependent analysis forcefully yielding an obvious issue of computation speed [28]. In the case of COMSOL and Simulink, the interaction is sequential, therefore there is no feedback from one solver to the next which can represent a limitation dealing with strongly coupled physics. This is the reason why, in the FEM, the homogenized **J-A** formulation is proposed to simulate the electromagnetic response of the machine to achieve the fastest possible computation speed to reduce the time burden induced by the co-simulation scheme.

To understand and catch some insights of the issues related to co-simulation, the subsequent work proposes to study a 15 MW superconducting hybrid synchronous generators having a HTS-wound rotor and a conventional stator interacting with a DC network, idealized as an infinite bus, via an AC/DC rectifier (AC for Alternating Current) and its RLC filter (RLC for Resistance-Inductance-Capacitor). The former is built as a FEM in COMSOL Multiphysics version 6.0 whereas the latter is simulated in the circuit simulator Simulink using Simscape Electrical [29]. The coupling between the software is done through the Functional Mock-up Unit (FMU) [30] which is simpler to use and as efficient as the early method introduced in [31]. First, a general introduction of the FEM of HTS machines and the formulations of the Maxwell equations are presented in section 2. The basis of the co-simulation is given in the subsequent section 3. In the next section 4, the methodology to study the machine and the system is detailed. It will be used for the analyses in section 6. The case study involving the connection of the generator to the external circuit is given in section 5. Appendices gather the key parameters for the case study and provide information on the electrical circuit analysis. It is concluded in section 7 that this methodology improves our understanding of electrical systems incorporating superconducting devices by offering further insights on the response of the machine coupled to a system as well as the system itself.

2. 2D FEM of superconducting rotating machine

The modeling of rotating machines is very often carried out in 2D using the finite element method to account for refined details of the cross-sectional geometries [32–34]. It is the case in the present work, considering racetrack coils for the HTS winding to accommodate thin, flat tapes. This configuration simplifies the design and provides an easy handling of the winding of tapes, preventing degradation arising from bending and twisting the HTS material [35].

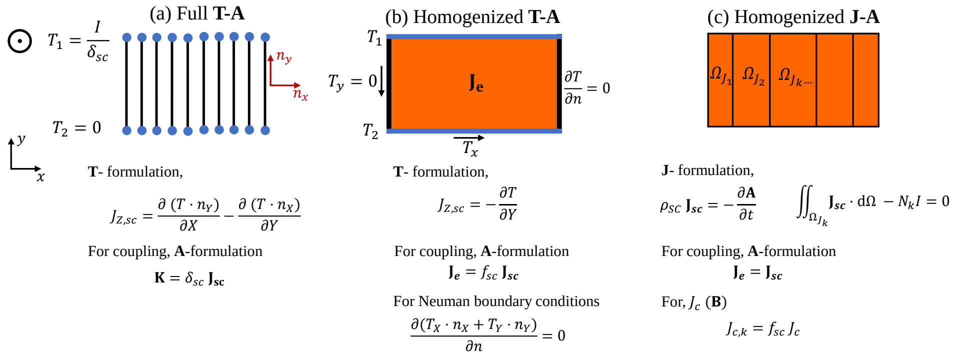

Figure 1. Summary of the implementation of the formulations in the 2D FEM of the HTS winding of the rotor [7,39]. Only the reference **T**-**A** formulation is presented in its full version. $J_{z,sc}$: z component of the current density flowing in the superconducting layer $\mathbf{J}_{sc}$; $\mathbf{K}$: surface current in [A/m] to impose the discontinuity of the field across the superconducting layer; δ_{sc}: thickness of the superconducting layer; $\mathbf{J}_e$: engineering current density; f_{sc}: fraction of superconductor in the winding; T_x and T_y, x and y components of the vector current potential $\mathbf{T}$; ρ_{sc}: resistivity of the superconductor; k: subscribed indicating the subdomain number; $N_k I$: Ampere-turns in the subdomain k; $\mathbf{J}_c$: critical current density; and, n_x and n_y: x and y components of the unit normal vector $\mathbf{n}$.

2.1. Generalities

The recent **T-A** formulation of the Maxwell equations has been successfully applied to the 2D FEM modeling of electrical rotating machines [21,36–38]. It is our formulation of reference to cross-check the latest **J-A** formulation. The **T** and **J** formulations leads to fast computation time solving the current density distribution in the HTS coils ($\mathbf{J} = \nabla \times \mathbf{T}$) whereas the **A** formulation solves the distribution of magnetic field over the entire machine according to $\mathbf{B} = \nabla \times \mathbf{A}$. In that regard, the **A** formulation is particularly useful to utilize the classic FEM techniques. It can simulate rotating machines using the moving mesh and it can easily incorporate the nonlinear virgin B-H curve of the ferromagnetic material. On this note, apart from the ferromagnetic cores, the remaining materials have a constant relative permeability equal to 1. The novelty of the approach is in the use of the **J-A** in the modelling of the rotating machine and its combination with homogenization technique to reduce further the computation time. For some machines, it is sometimes possible to decrease even more the computation time and the memory usage by using the symmetry arising from their design. However, the number of symmetries depends on the winding connections in conjunction with the relation between the number of slots in the stator and the number of poles in the rotor. For instance, in the present case study (see section 5), only 1 out of the 48 poles has been modeled.

To account for the relative motions of the rotor compared to the stator, two coordinate systems are introduced, a fixed one attached to the stator referred to as spatial frame (O,x,y) and a rotating one moving with the rotor at an angular velocity ω referred to as the material frame (O,X,Y) [7, 39]. These modeling capabilities are available in the AC/DC module of COMSOL.

2.2. $\mathbf{T}-\mathbf{A}$ *Formulation*

The **T-A** formulation has been recently applied in the modeling of superconducting electrical machines benefiting from the thin strip approximation arising from the layout of REBCO tapes [21, 36–38]. Fig. 1(a) and 1(b) summarizes the key features of the full and homogenized versions of the **T-A** formulation. The current vector potential **T**, related to the current density via $\mathbf{J} = \nabla \times \mathbf{T}$, is exclusively computed over the superconductor domain (Ω_{sc}). The magnetic field is solved over the entire domain via the magnetic vector potential **A** using second order elements [40].

The homogenized version of the **T-A** formulation implements a scaling of the current density flowing through the superconductor $\mathbf{J}_{sc}$. The resulting engineering current density $\mathbf{J}_e$ is defined as $\mathbf{J}_e = f_{sc}\mathbf{J}_{sc}$ with $f_{sc} = \delta_{sc}/\Delta_{sc}$, the scaling factor, where δ_{sc} is the thickness of the HTS layer and Δ_{sc} is the thickness of the tape including its insulation. Further details can be looked up in [18, 41].

2.3. $\mathbf{J}-\mathbf{A}$ *Formulation*

The **J-A** formulation is a mixed formulation [19] reading,

$$\rho_{sc}\,\mathbf{J}_{sc} = -\frac{\partial \mathbf{A}}{\partial t}, \tag{1}$$

where the state variable is the current density $\mathbf{J}_{sc}$ instead of current vector potential **T**. Thus far, the **J-A** formulation has been used to model superconducting tapes using a thin strip approximation [19] with zero element order in the **J** formulation and second order in **A** formulation simulating all the tapes (full model) [42]. In the present work, a new version of the **J-A** formulation is introduced that makes use of the homogenization technique to gain computation speed. In order to calculate accurately the current density distribution, the current must be imposed similarly to the homogenized version of the **H** formulation described in [20]. The stack of HTS tapes making the rotor is then subdivided in subdomains of different sizes. Thus, the outermost subdomains must be thinner than the innermost ones (see Fig. 1(c)) to catch the proper distribution of current density. The current is impressed as a point-wise constraint on the subdomain $\Omega_{J,k}$ as follows,

$$\iint_{\Omega_{J,k}} \mathbf{J}_{sc}\cdot \mathrm{d}\boldsymbol{\Omega} - N_k I = 0, \tag{2}$$

where $N_k I$ are the Ampere-turns corresponding to the number of superconducting tapes (N_k) in the subdomain $\Omega_{J,k}$ for a single tape current I. Additionally, the critical current density $J_{c,k}$ is scaled as $J_{c,k} = f_{sc}J_c$, where J_c is defined by (A.2) in Appendix A. The resistivity of the subdomain $\Omega_{J,k}$, $\rho_{sc,k}$, is described by (A.1) replacing the critical current density J_c by its scaled critical current density $J_{c,k}$. The power law model along with the Kim's relation are recalled in the same appendix.

For the specific case of a generator, a voltage is induced in the stator winding which arises from the temporal variation of **A** associated with the electrical conductivity of the stator winding σ. The magnetic vector potential is then solved over the entire domain via,

$$\nabla \times \frac{1}{\mu}\left(\nabla \times \mathbf{A}\right) + \sigma\partial_t\mathbf{A} = \mathbf{J}_e, \tag{3}$$

with $\mu = \mu_0$ for the "air" that encompasses the air-gap, the superconductor and the stator conductors; and, $\mu = \mu\left(B\right)$ for the ferromagnetic material.

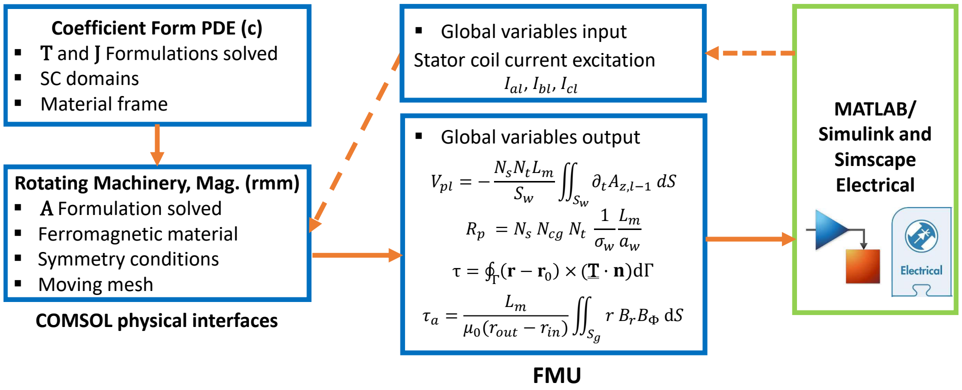

Figure 2. Schematic drawing of the coupling method between the FEM model in COMSOL and the electrical circuit in MATLAB/Simulink. Coefficient Form PDE (c) refers to the Partial Differential Equation module of COMSOL in its coefficient form denoted (c) on the domains for the homogeneous models and (cb) on the boundaries for the full model.

3. Co-simulation: coupling FEM-circuit

The coupling between COMSOL and Simulink is carried out using the Functional Mock-up Unit (FMU) interface built in Java. It allows to relate the discreet variables computed by COMSOL to the global variables in Simulink [28, 29], as illustrated in Fig. 2. Fig. 3 shows a diagram of the communication times between COMSOL and Simulink. The overall time stepping h_s is controlled by Simulink while COMSOL manages its own time step h_C, independently.

If p symbolizes the phases $\{a, b, c\}$, the mean voltage "V_{p_l}" induced in the stator winding of phase p and the corresponding series resistances "R_p" at the $l^{\text{th.}}$ number of communication steps are estimated in COMSOL. These global variables are subsequently sent to the circuit model as the following expressions,

$$V_{p_l} = -\frac{N_s N_t L_m}{S_w} \iint_{S_w} \partial_t A_{z,l-1} \mathrm{d}S, \tag{4}$$

and,

$$R_p = N_s N_{cg} N_t \frac{1}{\sigma_w} \frac{L_m}{a_w}, \tag{5}$$

where L_m is the axial length of the machine, N_t is the number of turns in the stator winding, S_w is the total cross-sectional area of the stator winding, σ is the conductivity of the conventional Cu stator, N_s is the number of sectors or symmetry, N_{cg} is the number of coil groups per phase, and a_w is the cross-sectional area of a single copper bar ($S_w = N_t N_{cg} a_w$). Hence, the machine is represented in the circuit model as an ideal controlled voltage source per phase (mean induced voltage V_{p_l}) in series with their respective phase resistance R_p. The phase current "I_{p_l}" is computed in the circuit simulator and it is given as input to COMSOL via the coil block interface. It is recalled that the subscript "l" refers to as the l^{th} communication step. The corresponding communication time interval is referred to as h_e. This communication time interval can be distinct from the time steps of the respective solvers. It represents the time difference between two instants at which both COMSOL and Simulink

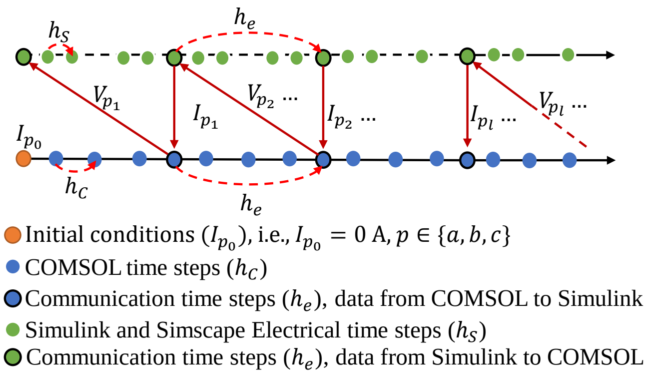

Figure 3. Time stepping process of the co-simulation.

exchange variables allowing both software to interact at fixed times in the transient simulation.

The Simulink ODE solver has the subsequent settings. The relative error on the solution for convergence is 10^{-6} and the time step is adaptive with a maximum time step set equal to the communication step h_e. The COMSOL solver time step is set to automatic with $h_C \leq h_e$ to ensure a better synchronization of the solvers. This constraint can be relaxed but the accuracy of the results lowers. By experience, trying out different combinations relating the communication time step and the time steps of the solvers, this setting has proven to be the most suitable to keep balance between a fair accuracy at a fast computation time.

4. Methodology to analyze the system

To understand the interaction of the machine with the system, the following parameters are estimated: electromagnetic torque (τ), voltages and currents, power, and harmonic distortions. These parameters yield information on the adequate design of the machine and the quality of the power supplied to the network. Some parameters are obtained from the FEM whereas others are computed from the circuit model. The following subsections are introducing those respective parameters. They are subsequently used to analyse the machine performance connected to a bus in the case study section 6.

4.1. Parameters obtained from the FEM

The electromagnetic torque is computed from the force acting on the rotor using the in-built 'Force Calculation' domain feature of COMSOL. The force is given by the integration of the Maxwell's stress tensor ($\underline{\underline{\mathbf{T}}}$) over the exterior boundaries of the rotor, shown as a red line in Fig. 4. The electromagnetic torque is then calculated from the force according to (6). The Maxwell's stress tensor encapsulates a comprehensive concept for generating magnetic stresses, forces, and torque. In numerical methods, the application of Maxwell's stress tensor is a common practice in the computation of forces and torque [43]. From the stress tensor, the torque is inferred as,

$$\tau = \oint_{\Gamma} (\mathbf{r} - \mathbf{r_0}) \times (\underline{\underline{\mathbf{T}}} \cdot \mathbf{n}) \, \mathrm{d}\Gamma, \qquad (6)$$

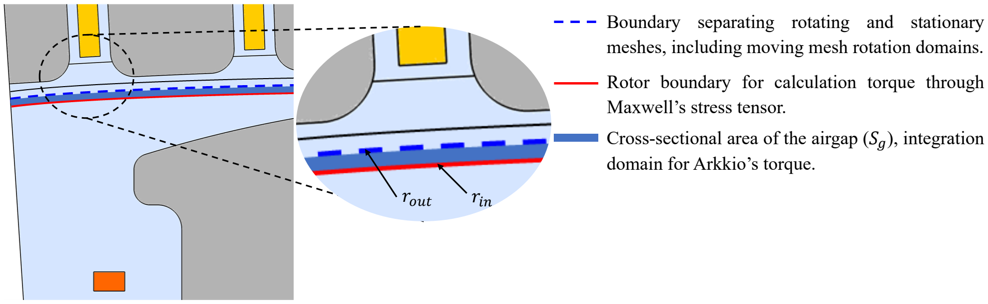

Figure 4. Schematic drawing defining the boundaries between the stator and the rotor. The air-gap region is divided in sub-regions. There, the blue line separating the rotating mesh from the static mesh does not coincide with the red line over which the torque is computed. This setting allows refining the mesh to compute the torque with greater accuracy independently of the moving interface for which the mesh finesse can be reduced.

where Γ is the enclosed surface around the rotor (red line in Fig. 4, situated in the air-gap domain at $\mu = \mu_0$ [43, 44]. Here, $\mathbf{r_0}$ is a point on the axis of rotation, located at the origin (0,0), and $\mathbf{n}$ is the outward normal unit vector to the Γ surface, parallel to the vector $\mathbf{r}$.

Despite the well established used of the Maxwell's stress tensor as mentioned previously, caution must be exercised on the accuracy of the results that can be greatly affected by the quality and fineness of the mesh. To cross-check the results, the Arkkio's method, available in COMSOL, has been used [45]. The advantage of the Arkkio's method is its low dependency on the mesh size and quality [46]. It integrates the torque over a fraction of the volume of the air-gap. This volume is squeezed between the radii r_{out} (rotating boundary for the moving mesh) and r_{in} (rotor domain boundary) as shown in Fig. 4 giving the following expression of the torque,

$$\tau_a = \frac{L_m}{\mu_0(r_{out} - r_{in})} \iint_{S_g} r\ B_r\ B_\Phi \mathrm{d}S, \tag{7}$$

in which B_r and B_Φ denote the radial and azimuthal flux densities over the surface $S_g = \pi\left(r_{out}^2 - r_{in}^2\right)$. To obtain the torque, both equations (6) and (7) must be multiplied by the number of symmetries (N_s) as only a fraction of the machine is simulated. The average electromagnetic torque and the definition of the torque ripple are given in Appendix B.

4.2. Parameters obtained from the electrical circuit

In nonlinear circuits, the waveform is not perfectly sinusoidal. Nonlinear loads create harmonic currents, which can be represented by Total Harmonic Distortion (THD). In this case, the apparent power (S) would be made up of three parts: the active power P, the reactive power Q, and the sum of all the powers generated by the distortion D (distortion component) [47, 48]. Details of the equations for powers and THD (voltage and current) are given in Appendix C and Appendix D, respectively.

The standard EN 50160:2010 [49] for power quality establishes limits for the THD, considering harmonics up to the 40 for standard cases and extending up to 50 for nonlinear loads. Here, this standard is not necessary applicable as all the

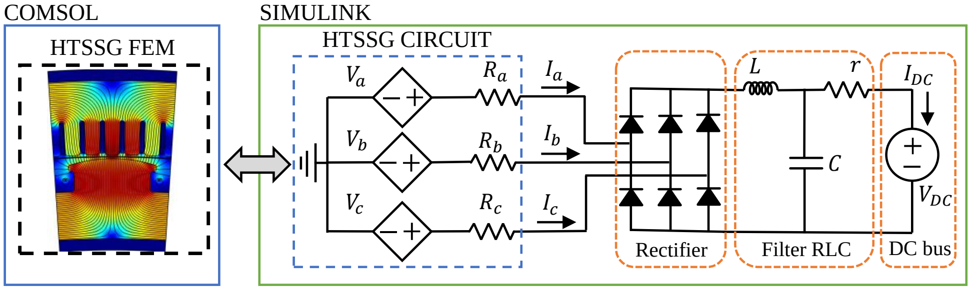

Figure 5. Electrical circuit simulated in Simscape electrical of Simulink. The machine is modeled as a FEM in COMSOL and represented in the electrical circuit by the induced voltages in the stator V_p in series with the winding resistances R_p for each phase p.

harmonics may not be reachable due to the discrete numerical computation. Indeed, a limit is given by the solvers' time step settings, $h_{s,max}$ and h_C, and in particular by the communication time step h_e when variables are exchanged between independent solvers. The maximum number of harmonics $N_{h,mx}$ is here determined on the basis of the minimum sampling rate given by the Nyquist-Shannon theorem to avoid aliasing. The theorem states that the signal should be sampled at a frequency at least twice the largest frequency present in the signal to prevent information loss [50]. In the present case, it is argued that the sampling is completely related to the communication time step. Hence, the maximum number of harmonics $N_{h,mx}$ that makes physical sense should fulfill the following requirement,

$$N_{h,mx} \leq \left\lfloor \frac{1}{\alpha h_e \nu} \right\rfloor . \tag{8}$$

α is a coefficient superior or equal to 2 according to the Nyquist theorem. In practice, the coefficient α can be larger than 2 to yield a better representation of the signals.

The harmonic analysis is carried out in MATLAB by computing the Discrete Fourier Transform (DFT) utilizing the Fast Fourier Transform algorithm (FFT). The data obtained from the co-simulation are assessed, comparing the voltage and current data from the Simulink electrical circuit data.

5. Case study

The case study involves a 15 MW HTS synchronous generator (HTSSG) coupled to a 6 kV DC network simulated as an "infinite" DC bus (ideal voltage source) through a rectifier and its associated RLC filter. Fig. 5 shows an overview of the case study, with the machine represented by the FEM coupled to the circuit. Subsequently, details of the pre-design of the machine for modeling purposes and the electrical circuit characteristics are presented.

5.1. Model of the 15 MW HTS synchronous generator (HTSSG) based on a pre-design

Fig. 6 shows the model layout of the 15 MW HTSSG. The topology is based on a salient pole synchronous machine. The hybrid HTSSG is made of a conventional Cu

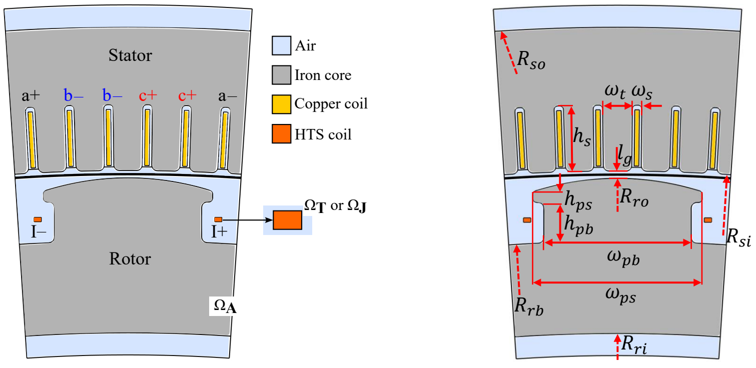

(a) (b)

Figure 6. 2D geometry of the HTS synchronous generator (HTSSG). (a) the three phases of the stator are labeled a, b and c. Benefiting from symmetry, 1 pole of the machine is modeled with the proper periodic boundary conditions. This is the condition of the case study presented in section 5. (b) geometrical parameters given in Table F1 of Appendix F.

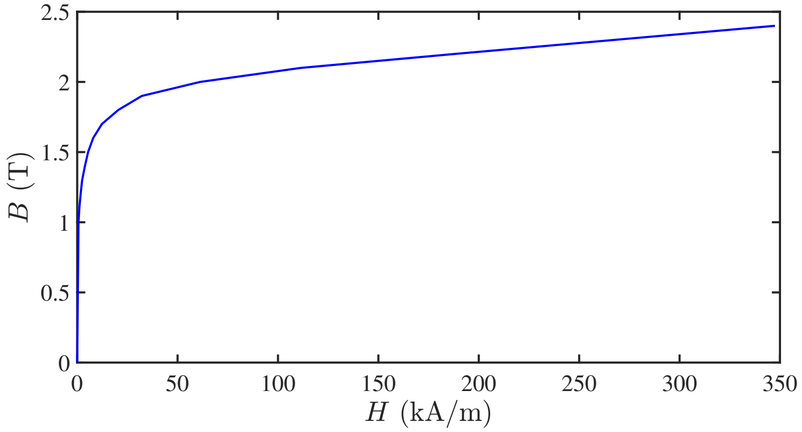

Figure 7. Virgin B-H curve: soft iron from COMSOL AC/DC Module material library [51].

stator and a rotor made of HTS racetrack coils. Each rotor coil is wound with 150 turns of insulated commercial Cu-stabilized REBCO tapes (12 mm wide, 0.13 mm thick) from Fujikura (FYSC-SCH12) [53]. The coils are operated at 60 K. The choice of the operating temperature is made on the basis of the power rating and a preset current margin. This point is detailed hereinafter. Here, the focus is not on the design of the machine and its associated cryogenic system. Hence, a pre-design of the machine is provided for only modeling purposes still ensuring the specified output power and some basic considerations such as the saturation of the ferromagnetic core. The latter can indeed impact the performance of the machine. Under these specifications, the machine has an outer radius of 5.098 m and a 48-pole, 288 slots holding a three-phase distributed winding made of insulated Cu wire ($6 \times 10^7\,\mathrm{S\,m^{-1}}$). The cores of the rotor and the stator are made of laminated ferromagnetic material whose B-H curve is given in Fig. 7. The complete sets of parameters for the HTS tape, including the

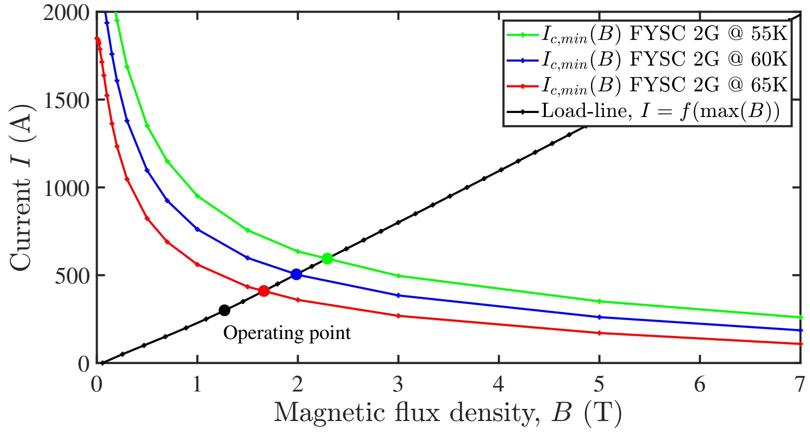

Figure 8. Determination of the operating temperature of the rotor winding for a given current margin equal to 60% of the minimum critical current ($I_{c,min}$) of the Fujikura FYSC 2G-HTS tape. The data were extracted from [52]. The critical current is equal to 595 A at 55 K [2.29 T], 505 A at 60 K [1.99 T], and 410 A at 65 K [1.67 T]. The optimal design is achieved for an operating temperature equal to 60 K. The loading curve is not linear due to the presence of the yoke.

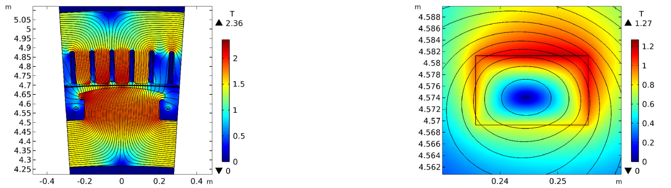

(a) (b)

Figure 9. Distribution of the magnetic flux density (B as norm of $\mathbf{B}$). (a) over the HTSSG machine and (b) a zoom out of the right HTS winding. The inhomogeneity of the distribution of B results from the presence of the iron yoke of the salient pole on the bottom and left sides of the HTS stack.

Kim's relation parameters of (A.2), and the machine are provided in Tables E1 and F1 of Appendix E and Appendix F, respectively.

During the pre-design phase, the critical current (I_c) of the HTS tape inside the winding is evaluated using the load-line method [54, 55]. The maximum value of the norm of the magnetic flux density $\mathbf{B}$ (the norm denoted as B) is evaluated over the stack of HTS tapes as a function of the current in the rotor. Here, a static computation is carried out with the rotor in a relative position compared to the stator yielding maximum magnetic flux on the rotor field winding (the worst case scenario). The relationship between the maximum field ($\max(B)$) and the current in the rotor corresponds to the load line ($I = f(\max(B))$). The dependence of the minimum critical current ($I_{c,min}$) on the magnetic field B for different temperatures is plotted alongside the load line, as depicted in Fig. 8. The data are found in the Robinson HTS Wire Critical Current Database for a commercial Fujikura FYSC 2G HTS tape [52]. The intersection of the load line and the $I_{c,min}$ as a function of the magnetic field

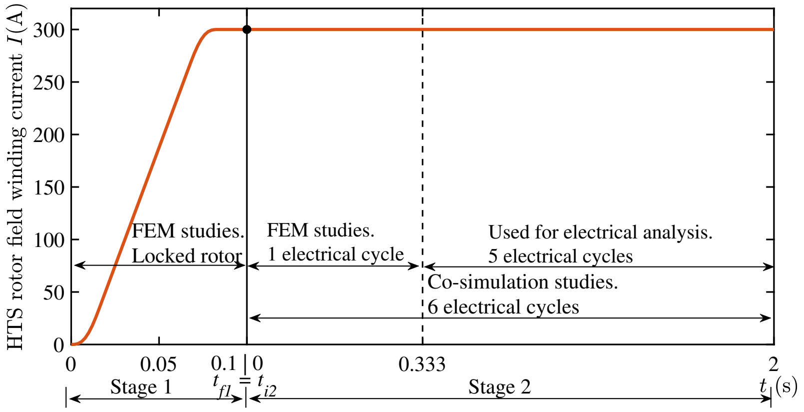

Figure 10. Simulation procedure. The current is first ramped in the HTS rotor coil at rest (stage 1); then a series of studies are carried out in stage 2 when the machine reaches steady state conditions. The first stage allows to initiate the conditions to run the co-simulation in stage 2. The x-axis is not to scale.

determines the I_c of the stack for a given operating temperature. This critical point is the basis to define the current margin for the rotor field winding. Here, a desired fraction of the critical current is about 60% yielding a margin of 40%. In the present case study, the operating temperature of 60 K fulfills the preset current margin of the HTS coil. The resulting critical current is equal to 505 A for a peak magnetic flux density B equal to 1.99 T on the stack. Taking the current margin of 40%, the rated current in the rotor is then 300 A. At this current, the perpendicular field reaches a maximum value of 1.275 T on the coil.

The stator saturates predominantly in the teeth (between 2.1 T and 2.2 T), and at the top corners of the salient poles (of the order of 2.36 T) still yielding an upper end of acceptable saturation for a HTS machine [56]. The distribution of the magnetic flux density was computed using the $\mathbf{A}$ formulation assuming a uniform current density in the HTS. The result for the static model is shown in Fig. 9 under nominal load. The inhomogeneity of the distribution of the magnetic flux density in the HTS rotor field comes from the presence of the salient pole surrounding part of the HTS stack. For the sides of the HTS stack close to the iron yoke, some of the flux lines are pulled away explaining the uneven distribution.

5.2. Power conversion and DC bus

The rectifier is composed of 6 power diodes 5SDD 75Y8500 manufactured by ABB. These diodes are modeled with a single slope. Their data-sheet characteristics are: $r_{on} = 0.118$ mΩ (resistance-on), $\sigma_{off} = 10$ nS (conductance-off) and $V_f = 0.945$ V (forward voltage). The passive filter consists of a shunt capacitor $C = 100$ mF, a series inductance $L = 15$ mH and a resistance $r = 0.13$ Ω. The rated DC bus voltage is 6 kV. Fig. 5 shows the circuit model implemented in Simulink. The three-phase stator of machine is represented by the induced phase voltages Vp with their series connected resistances. The parameters of the conversion system and the DC bus are compiled in Table G1 of Appendix G.

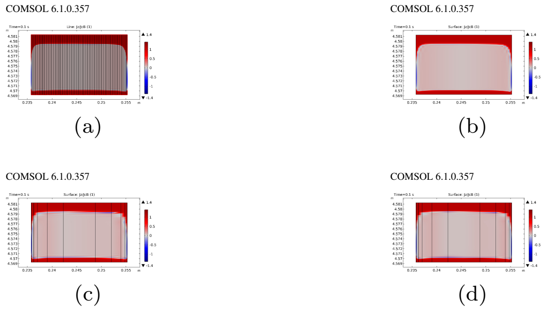

(a) (b)

(c) (d)

Figure 11. Normalized current density distribution ($J/J_c(\mathbf{B})$) over one HTS rotor field winding at $t_{f1} = 0.1$ s (modeling stage 1): (a) $\mathbf{T}_1$-$\mathbf{A}_2$ Full, (b) $\mathbf{T}_1$-$\mathbf{A}_2$ Hom., (c) $\mathbf{J}_1$-$\mathbf{A}_1$ Hom., (d) $\mathbf{J}_1$-$\mathbf{A}_2$ Hom..

6. Results of simulation

Before examining the system response, a first modeling stage was carried out using only the FEM. In this stage, the current was gradually ramped in the rotor field to its rated value equal to 300 A until a final time (here $t_{f1} = 0.1$ s) was reached. For this first modeling stage, the rotor is locked and the stator of the machine is not connected to any loads. Then, the final time t_{f1} is set as initial time t_{i2} for a second modeling stage (stage 2) where the machine is assumed in operation and the rotor is rotating. This second stage simulates more realistic operations. In this stage 2, two simulations are conducted: 1) a simulation using only the FEM in COMSOL and, 2) a co-simulation coupling sequentially the FEM in COMSOL and the electrical circuit in Simulink. The former simulation 1) uses the FEM alone to look at the performance of the machine. Thus, an open-circuit test and a test under load was simulated for a single power cycle. The second simulation 2) couples the FEM with the circuit to study the system in co-simulation. For this second more detailed modeling work, the global variables such as voltage, current, power and torque are compared for the same formulations when the machine reaches steady state with the rotor field current at its rated value.

The different modeling stages, referred to as modeling stage 1 and 2, are illustrated in Fig. 10. During stage 1, the current density distributes unevenly in the tapes and the stack. This unevenness will perdure in the steady state regime (stage 2) as long as there is no consequent changes in the operation of the machine that would lead to dissipation in the superconductor. It is thought as a more natural initial condition for stage 2 than a homogeneous distribution of current in the HTS stacks. This first stage, not having basis in the real operation of HTSSG, is simply used as initial condition for the second stage (stage 2) and it is run only once. All the required parameters are saved at time t_{f1} to run the additional simulations in stage 2.

All the studies were run on a personal laptop computer with an Intel® Xeon®E5 processor having 8 cores clocked at 3 GHz and 64-GB of DDRAM.

6.1. FEM results (modeling stage 1 and 2)

For the FEM results, the full **T-A** formulation was taken as reference. The idea is to estimate the variation of accuracy and computation times for the different formulations

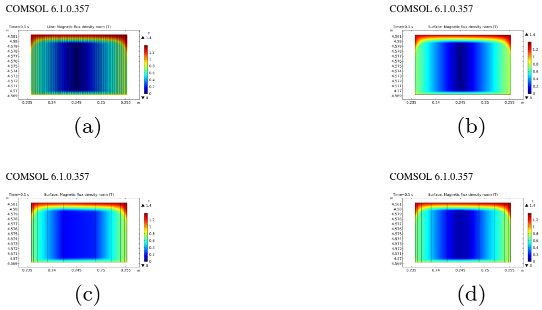

(a) (b)

(c) (d)

Figure 12. Magnetic flux density distribution (B as norm of $\mathbf{B}$) over one HTS rotor field winding at $t_{f1} = 0.1$ s (modeling stage 1): (a) $\mathbf{T}_1$-$\mathbf{A}_2$ Full, (b) $\mathbf{T}_1$-$\mathbf{A}_2$ Hom., (c) $\mathbf{J}_1$-$\mathbf{A}_1$ Hom., (d) $\mathbf{J}_1$-$\mathbf{A}_2$ Hom..

Table 1. 2D FEM results. Computation time and estimation of the accuracy using the coefficient of determination R^2 with the $\mathbf{T}$-$\mathbf{A}$ full as reference.

Formulations	Time			Mesh		DOF	R^2	
	Modeling stage 1	Modeling stage 2						
		Study (1): open-circuit	Study (2): Load	Elements	Edges		B	$J/J_c(\mathbf{B})$
$\mathbf{T}_1$-$\mathbf{A}_2$ Full	1 hr 58 min 33 s	15 min 8 s	25 min	59,774	20,263	139,788	Reference model	
$\mathbf{T}_1$-$\mathbf{A}_2$ Hom.	15 min 10 s	5 min 52 s	9 min 22 s	22,762	2,663	58,446	0.9966	0.9722
$\mathbf{J}_1$-$\mathbf{A}_1$ Hom.	1 min 44 s	2 min 11 s	4 min 54 s	19,500	3,747	12,537	0.9226	0.9663
$\mathbf{J}_1$-$\mathbf{A}_2$ Hom.	5 min 3 s	4 min 53 s	10 min 14 s	19,500	3,747	45,044	0.9941	0.9667

combined with homogenization technique compared to the reference formulation. The order of the elements representing the fields was adjusted to increase the accuracy of the results. For the $\mathbf{T}$-$\mathbf{A}$ formulations (homogenized and full), first order elements for the $\mathbf{T}$ field ($\mathbf{T}_1$) and second order elements for the $\mathbf{A}$ field ($\mathbf{A}_2$) were used as this combination provides the best accuracy. Table 1 summarizes the time computation, the parameters of the FEM and the accuracy for all the formulations. The subscripts 1 and 2 correspond to the order of elements. The slowest formulation is the full $\mathbf{T}$-$\mathbf{A}$ formulation. It is expected since all the HTS layers of the stacks are simulated. The best R^2 is given by the homogeneous model of the same reference formulation with a value of 0.9966 for B (norm of $\mathbf{B}$) and 0.9722 for J/J_c since all the tapes are simulated and more DOF (Degrees of Freedom) are solved. For both $\mathbf{J}$-$\mathbf{A}$ and $\mathbf{T}$-$\mathbf{A}$ formulations, a combination of element order can increase the accuracy. For the $\mathbf{J}$-$\mathbf{A}$ formulation, by using quadratic elements to represent the $\mathbf{A}$ field, the R^2 increases from a low 0.9226 with first order elements for B and 0.9663 for J/J_c to a reasonable 0.9941 and 0.9667, respectively. The poor accuracy on the J/J_c results directly from the fuzziness of the fronts of scaled current densities shown at the transition of the red color to the salmon color in Fig. 11. The latter presents the distribution of normalized current density ($J/J_c(\mathbf{B})$) over one stack of HTS tapes of the rotor field. The fuzziness is particularly noticeable at the top corners of the stack. On the contrary, this fuzziness is not present in the distribution of the magnetic flux density (norm of B) as shown in Fig. 12. Both figures are given at the final time of modeling stage 1 (t_{f1}) before initializing the co-simulation. As mentioned previously, the asymmetry of the distributions is due to the presence of the iron yoke on the bottom and left sides of the right stack illustrated in Fig. 6 and stressed out in Fig. 9. From these results obtained in the

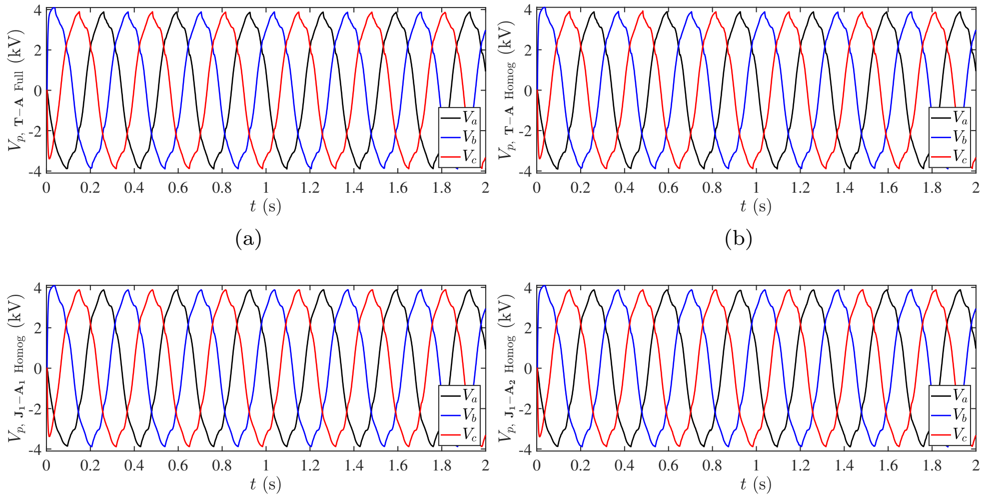

(a) (b)

(c) (d)

Figure 13. Phase voltages: (a) $\mathbf{T}_1$-$\mathbf{A}_2$ Full, (b) $\mathbf{T}_1$-$\mathbf{A}_2$ Hom., (c) $\mathbf{J}_1$-$\mathbf{A}_1$ Hom., (d) $\mathbf{J}_1$-$\mathbf{A}_2$ Hom..

modeling stage 1, the best formulation providing a fast response at a fair accuracy is the homogeneous **J-A** with second order elements for the **A** field. The fastest formulation is the homogeneous **J-A** one with first order element for both **T** and **A** fields. It would be the preferred choice for the system study but not necessarily for refining the design of the machine using the FEM.

Two additional studies were carried out in the modeling stage 2 using only the machine FEM. The first study (1) corresponds to an open-circuit test of the machine computing induced voltages and air gap flux distribution in the machine. The second study (2) was conducted at rated currents into the stator windings, phased 120° apart, to validate the magnitude of output power and to check the ripple of the electromagnetic torque. These tests were initiated at t_{2i} using the previous solutions of the FEM at t_{f1} for an additional power cycle. The results are also presented in Table 1 showing consistency of the computation time compared to the results of the current ramping (modeling stage 1).

6.2. Co-simulations results (modeling stage 2)

The co-simulation starts at time $t_{i2} = t_{f1}$ in the second stage, reset to $t_{i2} = 0$ s, for a duration of 2 s corresponding to $6/24^{\text{th}}$ of a complete rotation of the rotor (6 electrical cycles). It should be noted that the machine is operated at rated power at a constant rotation speed. The solutions of the distributed variables such as the current density and the magnetic vector potential obtained at time t_{f1} in the modeling stage 1 are loaded as initial conditions for the co-simulation in the modeling stage 2. The global parameters are set to zero leading to a quick transient before reaching steady state conditions.

The communication time step h_e between COMSOL and Simulink is equal to 3 ms. It corresponds to about 111 steps per electrical cycle yielding a sampling

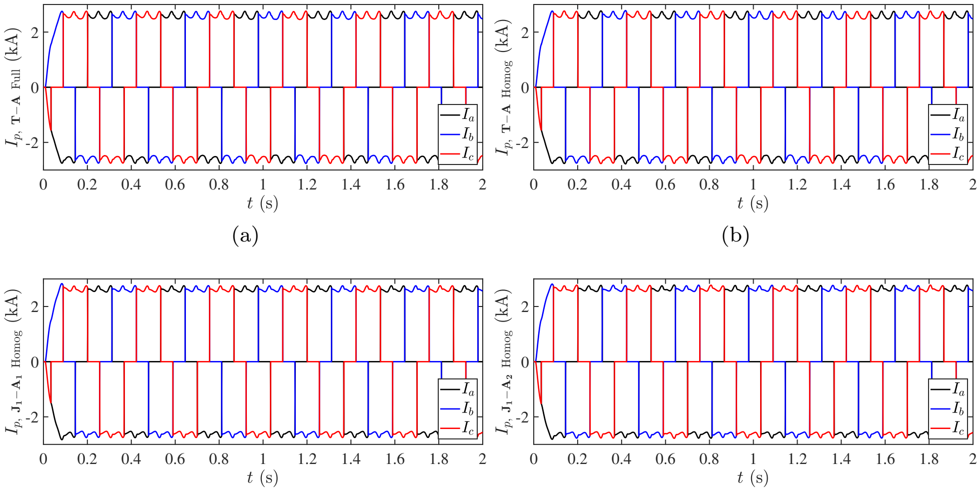

(a) (b)

(c) (d)

Figure 14. Phase currents: (a) $\mathbf{T}_1$-$\mathbf{A}_2$ Full, (b) $\mathbf{T}_1$-$\mathbf{A}_2$ Hom., (c) $\mathbf{J}_1$-$\mathbf{A}_1$ Hom., (d) $\mathbf{J}_1$-$\mathbf{A}_2$ Hom..

frequency of $f_s = 333.333$ S/s (Sample per second). Adhering to the Nyquist-Shannon theorem as introduced in section 4.2, this sampling rate adequately captures twice the maximum frequency equal to 166.66 Hz. In practical terms, it is typical to set $\alpha = 20$ in (8). Nonetheless, we chose a value of α equal to 10 in the present case. Indeed, this value allows catching enough harmonics to assess the machine operation, in particularly, the 7th harmonic that follows the fundamental flux. With $\alpha = 10$, up to 11 harmonics are included, the 11th corresponding to a frequency of 33 Hz. As a side note, the communication time step should be small enough to give flexibility on the coefficient α (always ≥ 2) to have sufficient odd harmonics in the voltage and current waveforms [57]. These harmonics impact the torque ripple and the overall machine performance. The goal is then to get a realistic representation of the frequency response of the machine to achieve an optimum design. For the analysis of the waveforms, only the last 5 electrical cycles ($n_{\text{cyc}} = 5$, i.e., $t_0 = 1/3$ s) are considered, covering a time range from 0.333 s to 2 s. The solver in Simulink is configured with variable time steps which do not exceed the communication time step h_e. The same settings as those used in the previous finite element analysis have been used for the COMSOL solver. In Simulink, the variable time step leads to the creation of several steps within the communication time step interval. Hence, over each communication time step h_e, the Simulink data are averaged so that the solutions are saved in a new set of isochronous times for their processing with the Fast Fourier Transform (FFT). This process is similar to filtering the signals therefore introducing a slight discrepancy between the raw data and the new data. The process leads to a maximum relative error in the Root Mean Square (RMS) values of voltages and currents of 2.16%.

In the present analysis, only the variables of the electrical circuit given by Simulink are examined. Throughout the analysis, the results for the three homogenized formulations of the Maxwell equations built in the FEM are compared with respect to

Table 2. Processing of the electrical parameters, voltage and current at the machine stator.

Parameters/Formulation	$\mathbf{T}-\mathbf{A}$ Full	$\mathbf{T}-\mathbf{A}$ Hom.		$\mathbf{J}_1$-$\mathbf{A}_1$ Hom.		$\mathbf{J}_1$-$\mathbf{A}_2$ Hom.	
	Values	Values	% ϵ_r	Values	% ϵ_r	Values	% ϵ_r
		Phase Voltages					
$V_{a,rms}$ phase a (V)	2733.90	2733.73	0.006%	2732.96	0.035%	2734.02	0.004%
$V_{b,rms}$ phase b (V)	2734.38	2734.26	0.004%	2734.06	0.012%	2734.44	0.002%
$V_{c,rms}$ phase c (V)	2734.08	2734.55	0.017%	2734.29	0.007%	2735.26	0.043%
		Phase Currents					
$I_{a,rms}$ phase a (A)	2114.64	2116.03	0.066%	2136.79	1.047%	2148.32	1.593%
$I_{b,rms}$ phase b (A)	2115.40	2117.92	0.119%	2140.05	1.166%	2149.79	1.626%
$I_{c,rms}$ phase c (A)	2115.21	2116.77	0.074%	2138.30	1.091%	2150.13	1.651%

Table 3. THD analysis of voltage and current waveforms for the three phases. The THD equations are given in Appendix C.

Parameters/Formulation	$\mathbf{T}-\mathbf{A}$ Full	$\mathbf{T}-\mathbf{A}$ Hom.		$\mathbf{J}_1$-$\mathbf{A}_1$ Hom.		$\mathbf{J}_1$-$\mathbf{A}_2$ Hom.	
	Values	Values [%]	% ϵ_r	Values [%]	% ϵ_r	Values [%]	% ϵ_r
		THD_v, phase voltages					
Phase a	7.406	7.403	0.040%	7.325	1.095%	7.349	0.771%
Phase b	7.439	7.440	0.002%	7.349	1.217%	7.384	0.741%
Phase c	7.452	7.454	0.029%	7.361	1.223%	7.410	0.563%
		THD_i, phase currents					
Phase a	26.551	26.554	0.012%	26.486	0.244%	26.523	0.104%
Phase b	26.377	26.357	0.077%	26.351	0.097%	26.353	0.088%
Phase c	26.504	26.508	0.017%	26.463	0.156%	26.355	0.561%

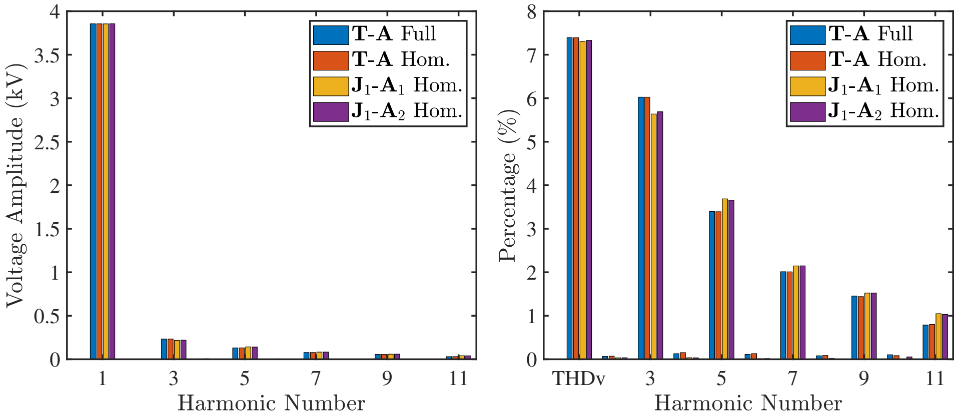

(a) (b)

Figure 15. Analysis of the harmonic content of phase 'a' voltage (V_a): (a) voltage amplitudes, (b) THD_v plus the percentage of the considered harmonic over the fundamental harmonic.

the **T-A** full model. Thus, Figs. 13 and 14 show the voltage and current waveforms at the stator of the HTSSG. The corresponding harmonics are given by Figs. 15 and 16. The harmonic analysis is carried out on phase 'a' starting from the fundamental $h = 1$ up to $N_{h,mx} = 11$. The total harmonic distortion (THD) is calculated with respect to the fundamental using (D.1) and (D.2) for voltage and current,

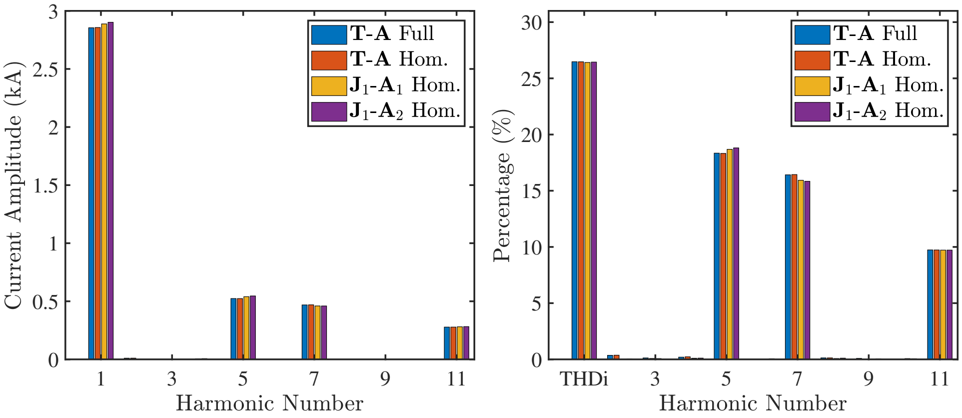

(a) (b)

Figure 16. Analysis of harmonic contents for phase 'a' current (i_a): (a) current amplitudes, (b) THD_i plus the percentage of the considered harmonic over the fundamental harmonic.

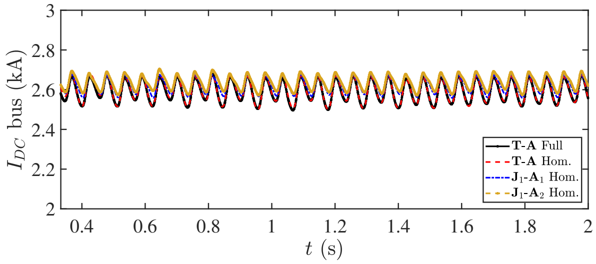

Figure 17. Current in the DC bus (I_{DC}).

respectively (see Appendix D). The voltage shows a large third harmonic whereas the corresponding harmonic of the current is negligible in comparison. It is expected since an imposed sinusoidal current is known to induce a large third harmonic in the voltage of a superconductor due to its nonlinearity as discussed in [58–60]. Table 2 compiles the rms values of the voltage and the current for the 3 phases. Table 3 shows their THD. The reference for the calculation of the relative error is chosen as the results of the **T-A** full model. The maximum relative error for the rms values comes from the homogenized $\mathbf{J}_1$-$\mathbf{A}_2$ formulation with 0.043% for the phase 'c' voltage and 1.651% for the phase 'c' current. The homogenized **T-A** formulation shows the best agreement with its full version as expected. The **J-A** formulations present the largest error in the rms currents for all the phases however the results are still acceptable with relative errors below 2%.

In the analysis of voltage THD, the linear $\mathbf{J}_1$-$\mathbf{A}_1$ formulation exhibits the maximum relative errors. The greatest error, equal to 1.223%, is observed in phase 'c' of the voltage when compared to the reference formulation **T-A** full, where THD_v is 7.452%. The highest harmonic components in the voltage are the odd harmonics as expected for rotating machine and the current harmonics are exclusively odd [57]. The highest relative error for the current is observed in the same phase 'c' equal to 0.561% for the $\mathbf{J}_1$-$\mathbf{A}_2$ formulation. There is no consistency between the peak

Table 4. Results on the machine performance. The equations for the torque and the powers are given in Appendix B and Appendix C, respectively.

Parameters/Formulation	$\mathbf{T}-\mathbf{A}$ Full	$\mathbf{T}-\mathbf{A}$ Hom.		$\mathbf{J}_1$-$\mathbf{A}_1$ Hom.		$\mathbf{J}_1$-$\mathbf{A}_2$ Hom.	
		Values	% ϵ_r	Values	% ϵ_r	Values	% ϵ_r
Electrical Parameters							
Apparent Power, S (MVA)	17.128	17.144	0.092%	17.326	1.154%	17.420	1.704%
Active Power, P (MW)	16.433	16.448	0.092%	16.633	1.217%	16.724	1.769%
Reactive Power, Q (MVAr)	-0.385	-0.391	1.522%	-0.371	3.581%	-0.379	1.558%
Distortion Power, D (MVAd)	4.815	4.818	0.074%	4.836	0.447%	4.861	0.965%
Factor Power (P/S)	0.9594	0.9594	0.001%	0.960	0.062%	0.960	0.064%
Performance Parameters							
Average torque, τ_{avg} (MN.m)	22.645	22.665	0.089%	22.665	0.089%	22.821	0.779%
Ripple torque, τ_{ripple}(%)	15.15	14.90	1.696%	15.38	1.485%	15.80	4.238%
Average inst 3-ph power, $P_{3ph,avg}$	16.321	16.347	0.159%	16.487	1.016%	16.553	1.417%
Average DC bus power $P_{DC,avg}$	15.692	15.694	0.016%	15.824	0.846%	15.915	1.423%

of relative errors across the **J-A** formulations. Overall, the results agree fairly well with the reference formulation with a relative error across all results of less than 2%. Given the THD, The distortion of the voltage waveform remains acceptable, especially considering a pre-design. The THD of the current in an uncontrolled three-phase full-wave rectifier is typically in the range of 30% to 40%. In the present case, a value of about 26% is computed. Consistent with the simulation results, the most significant harmonic components in the current occur for odd harmonics such as the fifth, seventh and then here the eleventh harmonics. These are non-multiples of 3 as expected. These harmonics are most prominent, the fifth corresponding to the braking torque and the seventh follows the fundamental of the rotating magnetic flux. These harmonics generate ripples in the torque. With a complete design, it would be possible to lower the harmonic content further and thus improve the values of THD_v and THD_i. Nevertheless, such a work is out of the scope of the present study. Indeed, the focus is on the methodology of the co-simulation presenting a variant of a new formulation of the Maxwell equation.

On the DC bus side, Fig. 17 shows ripples in the current I_{DC} with a ripple amplitude of less than 7.1%. These ripples are mainly controlled by the capacitor C of the RLC filter and directly impact the DC power given in Fig. 18(c). The instantaneous torque of the machine shown in Fig. 18(a) gives rise to the 3 phase power P_{3ph} given in Fig. 18(b). The torque presents reasonable oscillations to an amplitude of about 15% of the average torque. These oscillations arise from the distortion of the current waveform arising from the rectifier. The largest relative error is equal to 4.238% in the torque ripple for the homogenized $\mathbf{J}_1$-$\mathbf{A}_2$ formulation which is expected as it is the formulation showing the largest discrepancy in the phase currents. The post-processed values defining the machine performance are summarized in Table 4. The apparent power S, the active P and reactive powers Q as well as the distortion power D are computed for the different formulations (the corresponding equations are found in Appendix C). The distortion power is non negligible with an average across the results equal to 4.8 MVAd. The power factor is about 96%. For all these parameters, the relative error is below 4% across all the formulations with the largest relative error on the estimation of the reactive power for the $\mathbf{J}_1$-$\mathbf{A}_1$ homogenized model. On the DC bus side, an average of 15.78 MW flows in the system. It is less than the average AC active power of 16.56 MW generated by the machine.

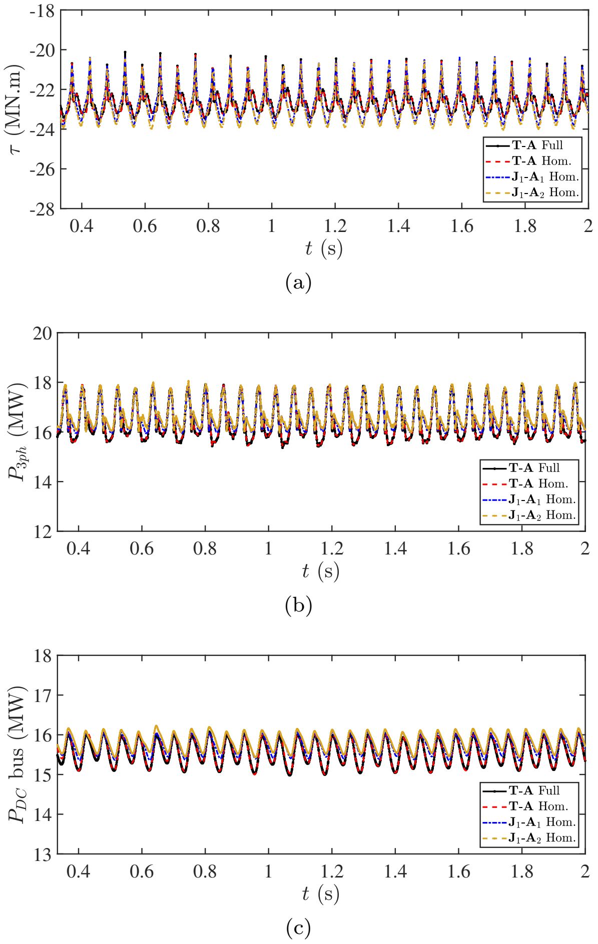

Figure 18. Comparisons of results obtained in co-simulation: (a) electromagnetic torque (τ), (b) instantaneous three-phase electrical power (P_{3ph}), and (c) electrical power supplied to the DC bus (P_{DC}).

The difference is explained by the chain of losses from the machine stator, passing by the rectifier and the filter before reaching the DC bus. Here, the conservation of energy is not guaranteed by the co-simulation since the solvers resolve sequentially the distributed and global variables. Hence, the choice of the communication time step and its relation with the solvers' time steps is crucial. The 3 ms time lapse is the largest admissible communication time step to still ensure the proper flow of power in the system. The overall losses amount of the system amounts to 629 kW for the reference full **T-A** formulation ($P_{3ph,avg} - P_{DC,avg}$, the average powers being defined in Appendix C).

Finally, Table 5 presents the computation time for all the formulations coupled with the electrical circuit in co-simulation. The reference model is the slowest with more than a day of computation time. This model shows the largest amount of degrees of freedom therefore the largest computation budget is required as illustrated by Table 1. The fastest model is given by the $\mathbf{J}_1$-$\mathbf{A}_1$ homogenized one. It ran in about

Table 5. Co-simulation time parameters and results for different communication steps.

Formulations	Time step (h_e=h_C)	No. steps per one electrical cycle FEM	Co-simulation time
$\mathbf{T}_1$-$\mathbf{A}_2$ Full	3[ms]	111	27 hrs 28 min
$\mathbf{T}_1$-$\mathbf{A}_2$ Hom.			13 h 51 min 31 s
$\mathbf{J}_1$-$\mathbf{A}_1$ Hom.			6 h 4 min 31 s
$\mathbf{J}_1$-$\mathbf{A}_2$ Hom.			13 h 7 min 40 s

6 h a little twice as fast as the same formulation but with second order elements in the **A** field. By increasing the order of the elements, the computation time get slower and slower. In summary, the computation time in co-simulation follows fairly the number of degrees of freedom in the FEM. In the present case, the Simulink model and its solver parameters are strictly the same for all the studies. It should be noted that the number of steps per electrical cycle may be increased to get a smaller communication time step and therefore a smaller time steps for the COMSOL solver in order to increase the resolution on the losses for instance. Here, 111 steps are enough to guarantee an accuracy below 5% on the electrical results at a very fast computation time but one cannot ensure that the AC losses of the HTS are of the same order.

7. Conclusion

The most recent formulations of the Maxwell equations for HTS machine modeling have been compared in co-simulation. The goal was to reduce the overall computation time working on the FEM as it is the model imposing the overall time computation. The reference formulation was chosen as the **T-A** full for its previous used in machine modeling and its fast computation time. This formulation was validated in the past against the well-established **H** formulation. A new version of the latest **J-A** have been introduced employing the homogenization technique. Similarly to the **T-A** formulation, second order elements are required in the **A** field to increase the accuracy on the distributed variables of the FEM such as the current density and magnetic flux density. However, such accuracy does not translate into a better accuracy when those formulations are coupled to electrical circuit in co-simulation. For the co-simulation, it was found that the formulation $\mathbf{J}_1$-$\mathbf{A}_1$ presents the fastest computation time with a peak relative error below 5% across all the estimated parameters of the machine and the system. Using this formulation combined with homogenization technique, it is possible to study in a reasonable time (a few hours) the performance of HTS machines connected to the network over several power cycles. Through the proposed harmonic analysis, the results of the behavior of the HTSSG in the system showed coherence with the results expected from the pre-design choice providing confidence on the validity of the method.

It is argued that the co-simulation is a step further to study along side equivalent models the performance of superconducting devices in practical electrical power systems. These systems involved complex circuitries such as power electronics that have nonlinear components relying on fast switching. It would then be intricate and computationally costly to build them within the same finite element software taking into account their realistic characteristics. Instead, it appears sensible to use the capability of different specialized software to get the best of both numerical tools.

This work showed an overview of the challenges of using co-simulation, in particular, the proper choice of the communication time steps between software. Thus, some rule of thumbs and a methodology have been promoted to ensure accurate and reliable results.

Acknowledgments

W. Durante-Gómez and F. Trillaud would like to thank the financial aid provided by the Dirección General de Asuntos del Personal Académico (DGAPA) of the National Autonomous University of Mexico (UNAM) through grant PAPIIT-2021 #IN108021. W. Durante-Gómez acknowledges the financial support from the Consejo Nacional de Humanidades, Ciencias y Tecnologías (CONAHCYT) via CVU: 867219.

References

[1] X. Song, C. Bührer, P. Brutsaert, J. Krause, A. Ammar, J. Wiezoreck, J. Hansen, A. V. Rebsdorf, M. Dhalle, A. Bergen, T. Winkler, S. Wessel, M. ter Brake, J. Kellers, H. Pütz, M. Bauer, H. Kyling, H. Boy, and E. Seitz. Designing and Basic Experimental Validation of the World's First MW-Class Direct-Drive Superconducting Wind Turbine Generator. *IEEE Transactions on Energy Conversion*, 34(4):2218–2225, 2019.

[2] X. Song, C. Bührer, A. Mølgaard, R. S. Andersen, P. Brutsaert, M. Bauer, J. Hansen, A. V. Rebsdorf, J. Kellers, T. Winkler, A. Bergen, M. Dhalle, S. Wessel, M. ter Brake, J. Wiezoreck, H. Kyling, H. Boy, and E. Seitz. Commissioning of the World's First Full-Scale MW-Class Superconducting Generator on a Direct Drive Wind Turbine. *IEEE Transactions on Energy Conversion*, 35(3):1697–1704, 2020.

[3] C. C. T. Chow, M. D. Ainslie, and K. T. Chau. High temperature superconducting rotating electrical machines: An overview. *Energy Reports*, 9:1124–1156, 2023.

[4] K. S. Haran, S. Kalsi, T. Arndt, H. Karmaker, R. Badcock, B. Buckley, T. Haugan, M. Izumi, D. Loder, J. W, Bray. High power density superconducting rotating machines—development status and technology roadmap. *Superconductor Science and Technology*, 30(12):123002 (41pp), 2017.

[5] A. Bergen *et al.* Design and in-field testing of the world's first ReBCO rotor for a 3.6 MW wind generator. *Superconductor Science and Technology*, 32:125006, 2019.

[6] A. Baez-Muñoz, F. Trillaud, J. R. Rodriguez-Rodriguez, L. M. Castro, and R. Escarela-Perez. Thermoelectromagnetic lumped-parameter model of high temperature superconductor generators for transient stability analysis. *IEEE Transactions on Applied Superconductivity*, 31(5):1–5, 2021.

[7] R. Brambilla, F. Grilli, L. Martini, M. Bocchi, and G. Angeli. A finite-element method framework for modeling rotating machines with superconducting windings. *IEEE Transactions on Applied Superconductivity*, 28(5):1–11, 2018.

[8] F. Liang, S. Venuturumilli, H. Zhang, M. Zhang, J. Kvitkovic, S. Pamidi, Y. Wang, and W. Yuan. A finite element model for simulating second generation high temperature superconducting coils/stacks with large number of turns. *Journal of Applied Physics*, 122(4):043903 (10pp), 2017.

[9] ANSYS, Inc. Ansys electronics electromagnetic, signal integrity, thermal and electro-mechanical simulation solutions, 2023.

[10] Altair Engineering, Inc. Altair® Flux® Applications, 2023.

[11] JMAG International. JMAG-RT, 2023.

[12] W. Liang, J. Wang, T. Lu, and W. Fang. A new method for multiple finite - element models in cosimulation with electrical circuit using machine multiloop modeling scheme. *IEEE Transactions on Industrial Electronics*, 61(12):6583–6590, 2014.

[13] V. Varvolik, D. Prystupa, G. Buticchi, S. Peresada, M. Galea, S. Bozhko. Co-simulation analysis for performance prediction of synchronous reluctance drives. *Electronics*, 10(2154):16pp, 2021.

[14] M. Hsieh, C. Lin and I. Lin. Design and Analysis of High Temperature Superconducting

Generator for Offshore Wind Turbines. *IEEE Transactions on Magnetics*, 49(5):1881–1884, 2013.

[15] L. Wang and Y. Chen. An efficient HTS electromagnetic model combining thin-strip, homogeneous and multi-scale methods by T-A formulation. *Cryogenics*, 124:103469, 2022.

[16] J. Dular, K. Berger, C. Geuzaine, and B. Vanderheyden. What Formulation Should One Choose for Modeling a 3-D HTS Motor Pole With Ferromagnetic Materials? *IEEE Transactions on Magnetics*, 58(9):1–4, 2022.

[17] H. Zhang, M. Zhang, and W. Yuan. An efficient 3D finite element method model based on the T–A formulation for superconducting coated conductors. *Supercond. Sci. Technol.*, 30(2):024005, 2016.

[18] E. Berrospe-Juarez, V. M. R. Zermeño, F. Trillaud, and F. Grilli. Real-time simulation of large-scale HTS systems: multi-scale and homogeneous models using the T–A formulation. *Superconductor Science and Technology*, 32(6):065003, apr 2019.

[19] G. dos Santos, B. M. Oliveira Santos, F. Sass, F. Goulart dos Reis Martins, G. Gonçalves Sotelo, and R. de Andrade Junior. J-a formulation: A finite element methodology for simulating superconducting devices. *Superconductivity*, 6:100049, 2023.

[20] Edgar Berrospe-Juarez, Frederic Trillaud, Víctor M R Zermeño, and Francesco Grilli. Advanced electromagnetic modeling of large-scale high-temperature superconductor systems based on *H* and *T-A* formulations. *Superconductor Science and Technology*, 34(4):044002, feb 2021.

[21] X. Huang, Z. Huang, X. Xu, L. Wang, W. Li and Z. Jin. A Fully Coupled Numerical Method for Coated Conductor HTS Coils in HTS Generators. *IEEE Transactions on Applied Superconductivity*, 30(4):5206406 (6pp), 2020.

[22] M. Boll, M. Corduan, S. Biser, M. Filipenko, Q. Huang Pham, S. Schlachter, P. Rostek and M. Noe. Simulation of AC Loss in the Armature Windings of a 100 kW All-HTS Motor With Various (RE)BCO Conductor Considerations. *Supercond. Sci. Technol.*, 33(4):044014 (14pp), 2019.

[23] P. Zhou, G. Dos Santos, A. Ghabeli, F. Grilli, and G. Ma. Coupling electromagnetic numerical models of HTS coils to electrical circuits: multi-scale and homogeneous methodologies using the T-A formulation. *Superconductor Science and Technology*, 35(11):115005, 10 2022.

[24] G dos Santos, F G R Martins, F Sass, D H N Dias, G G Sotelo, and A Morandi. A coupling method of the superconducting devices modeled by finite element method with the lumped parameters electrical circuit. *Superconductor Science and Technology*, 34(4):045014, 3 2021.

[25] B. M. Oliveira Santos, G. dos Santos, F. Sirois, R. Brambilla, R. de Andrade Junior, F. Sass, G. Gonçalves Sotelo, and F. Grilli. 2-D Modeling of HTS Coils With *T-A* Formulation: How to Handle Different Coupling Scenarios. *IEEE Transactions on Applied Superconductivity*, 32(5):1–4, 2022.

[26] G. dos Santos, B. M. Oliveira Santos, F. Goulart dos Reis Martins, F. Sass, G. Gonçalves Sotelo, and R. de Andrade. An integrated methodology to assess ac losses in the khz range using the fem and partial element equivalent circuit. *IEEE Transactions on Applied Superconductivity*, 32(2):1–8, 2022.

[27] G. Hajiri, K. Berger, F. Trillaud, J. Lévêque, and H. Caron. Impact of Superconducting Cables on a DC Railway Network. *Energies*, 16(2), 2023.

[28] A. Dahash, F. Ochs, and A. Tosatto. Co-simulation of dynamic energy system simulation and COMSOL multiphysics®. *COMSOL Conference, Cambridge*, 2019.

[29] COMSOL Multiphysics. Integrate comsol multiphysics® into simulink® with livelink™ for simulink®, 2023.

[30] Z. Wang, L. Ren, Y. Tang, S. Yan, Y. Xu, K. Gong, and X. Deng. A Coupling Simulation and Modeling Method for High Temperature Superconducting Magnets. *IEEE Transactions on Applied Superconductivity*, 27(4):1–5, 2017.

[31] A. W. M. van Schijndel. Implementation of comsol in simuLink S-functions, revisited. *Proceedings of the Comsol Conference Cambridge*, pages 1–7, 17-19 September 2014.

[32] S. J. Salon. *Finite Element Analysis of Electrical Machines (Power electronics and Power Systems)*. Springer, 2012.

[33] M. Curti, J. J. H. Paulides, and E. A. Lomonova. An overview of analytical methods for magnetic field computation. *2015 Tenth International Conference on Ecological Vehicles and Renewable Energies (EVER)*, pages 1–7, 2015.

[34] B. Stoev, G. Todorov, P. Rizov, G. Pagiatakis, and L. Dritsas. Finite element analysis of rotating electrical machines — an educational approach. In *2017 IEEE Global Engineering Education Conference (EDUCON)*, pages 262–269, 2017.

[35] X. Li, Z. Yang, Y. Xu, L. Ren, H. Zhang, X. Ding, and Y. Tang. Effects of bending and torsion behavior on Ic degradation and microstructure of ReBCO coated conductors. *Cryogenics*,

126:103523, 2022.

[36] T. Benkel, M. Lao, Mayraluna, Y. Liu, E. Pardo, S. Wolfstädter, T. Reis, F. Grilli. T–A-Formulation to Model Electrical Machines With HTS Coated Conductor Coils. *IEEE Transactions on Applied Superconductivity*, 30(6):5205807 (7pp), 2020.

[37] C. R. Vargas-Llanos, S. Lengsfeld, and F. Grilli. T-A Formulation for the Design and AC Loss Calculation of a Superconducting Generator for a 10 MW Wind Turbine. *IEEE Access*, 8:208767–208778, 2020.

[38] Y. Yang, H. Yong, X. Zhang and Y. Zhou. Numerical Simulation of Superconducting Generator Based on the T–A Formulation. *IEEE Transactions on Applied Superconductivity*, 30(8):5207611 (11pp), 2020.

[39] A. Ferrario. How to model rotating machinery in 3d, Apr 2015.

[40] J. Dular, M. Harutyunyan, L. Bortot, S. Schöps, B. Vanderheyden, and C. Geuzaine. On the stability of mixed finite-element formulations for high-temperature superconductors. *IEEE Transactions on Applied Superconductivity*, 31(6):1–12, 2021.

[41] F. Huber, W. Song, M. Zhang and F. Grilli. The T-A formulation: an efficient approach to model the macroscopic electromagnetic behaviour of HTS coated conductor applications. *Supercond. Sci. Technol.*, 35(4):x043003, 2022.

[42] S. Wang, H. Yong, and Y. Zhou. Numerical calculations of high temperature superconductors with the J-A formulation. *Superconductor Science and Technology*, 36(11):115020, sep 2023.

[43] J. Pyrhonen, T. Jokinen, and V. Hrabovcova. *Design of rotating electrical machines.* John Wiley & Sons, 2013.

[44] J. P. A. Bastos and N. Sadowski. *Electromagnetic modeling by finite element methods.* CRC press, 2003.

[45] A. Arkkio. *Analysis of induction motors based on the numerical solution of the magnetic field and circuit equations.* Helsinki University of Technology, 1987.

[46] N. Sadowski, Y. Lefevre, M. Lajoie-Mazenc, and J. Cros. Finite element torque calculation in electrical machines while considering the movement. *IEEE Transactions on Magnetics*, 28(2):1410–1413, 1992.

[47] A. A. P. Miguel, F. Eddi, J. P. Cinotti, and É. Regimbeau. *La menace des harmoniques: mesure, analyse et solutions.* MGE UPS Systems, 2000.

[48] C. Kocatepe, R. Yumurtacı, O. Arıkan, M. Baysal, B. Kekezoglu, A. Bozkurt, and C. F. Kumru. *Harmonic effects of power system loads: An experimental study.* IntechOpen, 2013.

[49] EN Standard. 50160: 2010: Voltage characteristics of electricity supplied by public distribution systems. *Slovenski Standard: Ljubljana, Slovenija*, 2010.

[50] J. G. Proakis and D. G. Manolakis. *Digital Signal Processing.* Pearson custom library. Pearson, 2013.

[51] COMSOL. COMSOL Multiphysics version 6.0. `https://www.comsol.com/`, 2021.

[52] Robinson Research Institute, Victoria University of Wellington. Robinson HTS Wire Critical Current Database, Fujikura FYSC 2G HTS. `https://htsdb.wimbush.eu/dataset/3759321`, 2023.

[53] Fujikura Europe Ltd. 2G-REBCO-High Temperature Superconductors. `https://www.fujikura.co.uk/`, 2023.

[54] Y. Xu, L. An, B. Jia, and N. Maki. Study on electrical design of large-capacity fully superconducting offshore wind turbine generators. *IEEE Transactions on Applied Superconductivity*, 31(5):1–5, 2021.

[55] Y. Liu, F. Grilli, J. Cao, L. Li, C. Zhang, M. Wang, F. Xu, J. Lin, and M. Noe. An electromagnetic design of a fully superconducting generator for wind application. *Energies*, 14(22), 2021.

[56] D. S. Dezhin, R. I. Ilyasov, and K. L. Kovalev. Hts inductor electric machine with combined excitation. *IOP Conference Series: Earth and Environmental Science*, 194(5):052007, nov 2018.

[57] G. J. Wakileh. Harmonics in rotating machines. *Electric Power Systems Research*, 66(1):31–37, 2003.

[58] L. Ji, R. H. Sohn, G. C. Spalding, C. J. Lobb, and M. Tinkham. Critical-state model for harmonic generation in high-temperature superconductors. *Phys. Rev. B*, 40:10936–10945, Dec 1989.

[59] Y. Mawatari, H. Yamasaki, and Y. Nakagawa. Theoretical investigation on 3rd harmonic voltage in inductive measurements of critical current density in superconducting films. *IEEE Transactions on Applied Superconductivity*, 13(2):3710–3713, 2003.

[60] T. Nadami, E.S. Otabe, M. Kiuchi, T. Matsushita, Y. Mawatari, H. Yamasaki, and Y. Nakagawa. Numerical calculation of third harmonic voltage induced by a shielding

current in a superconducting thick film. *Physica C: Superconductivity*, 426-431:688–692, 2005. Proceedings of the 17th International Symposium on Superconductivity (ISS 2004).

[61] J. Rhyner. Magnetic properties and AC-losses of superconductors with power law current—voltage characteristics. *Physica C: Superconductivity*, 212(3):292–300, 1993.

[62] Y. Zhai, G. Ma, J. Li, P. Zhou, G. Ren, and Y. Zhou. Numerical study for the impact of current sharing effect upon dynamic behaviour of DC-carrying HTS coils under alternating magnetic fields. *Cryogenics*, 135:103730, 2023.

[63] E. F. Fuchs and M. A. S. Masoum, editors. *Chapter 1 - Introduction to Power Quality.* Academic Press, Burlington, 2008.

[64] M. Park H.-J. Sung and I.-K. Yu. Designs of 10 mw air-core and iron-core hts wind power generators. *J. Electr. Eng. Technol.*, 10(2):545–550, 2015.

[65] S. Wimbush, N. Strickland, A. Pantoja. Critical current characterisation of Fujikura FYSC 2G HTS superconducting wire. `https://figshare.com/articles/dataset/Critical\_current\_characterisation\_of\_Fujikura\_2G\_HTS\_superconducting\\_wire/3759321/2`, 2023.

Appendix A. Resistivity model of the superconductor

For both formulations, the electrical resistivity of the superconductor (ρ_{sc}) is given by the following E-J power-law relation [61],

$$\rho_{sc} = \frac{E_c}{J_c(\mathbf{B})}\left|\frac{\mathbf{J}}{J_c(\mathbf{B})}\right|^{n-1}. \tag{A.1}$$

E_c is the critical electric field, typically equal to $1\,\mu\mathrm{V/cm}$, and n is the transition index. In this model, the critical current density J_c is defined by a modified Kim's relation [62] to account for the impact of the magnetic field on the electromagnetic behavior of the tape, so that,

$$J_c(\mathbf{B}) = \frac{J_{c0}}{\left(1 + \dfrac{\sqrt{k^2 B_\parallel^2 + B_\perp^2}}{B_0}\right)^{\alpha}}, \tag{A.2}$$

where $B_\perp$ and $B_\parallel$ are the magnetic field components perpendicular and parallel to the wide tape surface, i.e. $B_\perp = B_x$ and $B_\parallel = B_y$ in Fig. 1. k, B_0, and α represent the parameters used for fitting the critical current curve to the experimental data, while J_{c0} is the critical current density in the absence of an external magnetic field at a reference temperature, usually the rated operating temperature.

At the operating temperature, the critical current is computed from the critical current density as $I_c = A_{sc}J_c$, where A_{sc} is the cross-section of the superconductor layer.

Appendix B. Average torque and torque ripple

The average of the electromagnetic torque is given by,

$$\tau_{avg} = \frac{1}{n_{cyc}T_p}\int_{t_0}^{t_0+n_{cyc}T_p} \tau(t)\,dt, \tag{B.1}$$

where T_p denotes the period of the electrical cycle of the machine and n_{cyc} represents the number of electrical cycles considered in the evaluation. The time t_0 is an initial time of integration. The torque ripple is defined as the percentage of the difference between the maximum torque $\tau_{\max}$ and the minimum torque $\tau_{\min}$ relative to the average torque τ_{avg} over the n_{cyc} electrical cycles. It is given by the following expression,

$$\tau_{\text{ripple}} = \left(\frac{\tau_{\max} - \tau_{\min}}{\tau_{avg}} \right) \times 100. \tag{B.2}$$

Appendix C. Computation of powers: S, P, Q and D

The squared norm of the apparent power is then given by,

$$S^2 = P^2 + Q^2 + D^2. \tag{C.1}$$

The calculation of the different powers is carried out by decomposing the signals in their harmonics. The active and reactive powers are then computed as [63],

$$P = V_{av} I_{av} + \sum_{h=1}^{+\infty} V_h \ I_h \cos\left(\theta_h\right), \tag{C.2}$$

and,

$$Q = \sum_{h=1}^{+\infty} V_h \ I_h \sin\left(\theta_h\right). \tag{C.3}$$

The apparent power is computed as,

$$S = V_{rms} \ I_{rms} = \sqrt{\left(\sum_{h=0}^{+\infty} V_h^2 \right) \left(\sum_{h=0}^{+\infty} I_h^2 \right)}. \tag{C.4}$$

V_{av} and I_{av} represent the average values or the DC component (not to confound with the values of the DC bus shown in the case study); V_h and I_h denote the harmonic voltages and currents with the subscript "1" indicating the fundamental. θ_h represents the phase shift between the voltage and current angles for each harmonic component, defined as $\theta_h = \theta_{v,h} - \theta_{i,h} = N_h 2\pi\nu$, with ν the frequency of the induced voltage in the stator and N_h the harmonic number. The distortion component is obtained from (C.1).

The average electrical power of the DC bus is computed from the instantaneous DC power $P_{DC}(t) = I_{DC}(t) \cdot V_{DC}(t)$ as follows,

$$P_{DC,avg} = \frac{1}{n_{cyc}T} \int_{t_0}^{t_0 + n_{cyc}T} P_{DC}(t)\, dt, \tag{C.5}$$

Additionally, the average three-phase electrical power, calculated from the measured instantaneous three-phase power $P_{3ph}(t) = V_a(t) \cdot I_a(t) + V_b(t) \cdot I_b(t) + V_c(t) \cdot I_c(t)$ prior to rectifier coupling, is inferred as,

$$P_{3ph,avg} = \frac{1}{n_{cyc}T} \int_{t_0}^{t_0 + n_{cyc}T} P_{3ph}(t)\, dt. \tag{C.6}$$

The time integration of instantaneous three-phase electrical power over the desired period, averaged across n_{cyc} complete electrical cycles, yields the active power. This estimation is valid for balanced systems but it remains a first approximation. Indeed, it does not include all the harmonics to compute accurately the active power as defined by (C.2).

Table E1. Characteristics of the REBCO commercial tape at 60 K [52, 65].

Parameters	Value
HTS tape	
HTS tapes	Fujikura FYSC 2G [53]
Tape width	12 mm
HTS layer thickness	2 μm
Tape thickness	0.13 mm
Critical electric field (E_c)	$1\,\mu$V/cm
Transition index (n)	30
Self-field critical current density (J_{c0})	9.427×10^{10} A/m^2
Kim's relation	
Anisotropy factor (k)	0.6075
Reference field, B_0	0.1 T
Power factor, α	0.4415

Appendix D. Total Harmonic Distortion: THD

The THD represents the cumulative effect of all harmonics evaluated up to the $N_{h,mx}$ multiple of the fundamental frequency of the power system [64]. For the voltage and current waveforms, it reads,

$$THD_V\,[\%] = \frac{100}{V_1}\sqrt{\sum_{h=2}^{N_{h,mx}} V_h^2}, \tag{D.1}$$

and,

$$THD_I\,[\%] = \frac{100}{I_1}\sqrt{\sum_{h=2}^{N_{h,mx}} I_h^2}. \tag{D.2}$$

Appendix E. Parameters of the HTS tape

Table E1 summarizes the superconducting characteristics of the commercial REBCO tape and the parameters of the Kim's relation (A.2) at the operating temperature.

Appendix F. Parameters of the 15 MW HTSSG

Table F1 compiles the main parameters of the generator and the HTS coil rotor.

Appendix G. Parameters of the DC bus electric circuit (rectifier and filter)

Table G1 summarizes the parameters of the conversion system and the DC bus.

Table F1. Characteristics of the 15 MW HTSSG. Pre-design parameters for wind power application.

Parameters	Value
Machine	
Electrical Power (P)	15 MW
Line voltage (V_L)	4.77 kV
Line current (I_L)	1.815 kA
No. of phases	3
Electrical frequency (f_e)	3 Hz
No. of poles	48
No. of slots	288
Rotor mechanical speed (η)	7.5 rpm
Machine geometric parameters	
Inner rotor radius (R_{ri})	4.2675 m
Rotor back iron radius (R_{rb})	4.5175 m
Outer rotor radius (R_{ro})	4.6885 m
Inner stator radius (R_{si})	4.7085 m
Outer stator radius (R_{so})	5.0985 m
Length of the machine (L_m)	1.9 m
Air gap length (l_g)	20 mm
Tooth width (ω_t)	77.043 mm
Slot width (ω_s)	25.681 mm
Slot height (h_s)	180 mm
Number of turns in the stator winding (Cu bars)	4
Dimensions of a single Cu bar	1.27 cm × 3.81 cm (1/2" × 1.5")
Pole body height (h_{pb})	115.44 mm
Pole shoes straight-section height (h_{ps})	29.303 mm
Pole body width (ω_{pb})	400.29 mm
Pole shoes width (ω_{ps})	460.11 mm
HTS coil rotor	
No. of tapes per coil	150
Rotor operating temperature	60 K
Rated current / critical current (I / I_c)	300 A / 502 A

Table G1. Parameters of the DC bus electric circuit (rectifier and RLC filter).

Parameter	Value
Stator winding resistance ($R_{a,b,c}$)	25.131 mΩ
Rectifier	
Power diodes	5SDD 75Y8500
On resistance (r_{on})	0.118 mΩ
Conductance ($1/r_{off}$)	10 nS
Forward voltage (V_f)	0.945 V
Filter RLC	
Resistor (r)	0.13 Ω
Inductor (L)	15 mH
Capacitor (C)	100 mF
DC Voltage source (V_{DC})	6 kV